Title

X-ray Linear Dichroism in Apatite

Journal

Journal of the American Chemical Society, 140(37)

ISSN

0002-7863

Authors

Stifler, Cayla A

Wittig, Nina Kølln

Sassi, Michel

et al.

Publication Date

2018-09-19

DOI

10.1021/jacs.8b05547

Peer reviewed

JACS
JOURNAL OF THE AMERICAN CHEMICAL SOCIETY
Article
Cite This: J. Am. Chem. Soc. XXXX, XXX, XXX−XXX
pubs.acs.org/JACS

X-ray Linear Dichroism in Apatite

Cayla A. Stifler,[†] Nina Kølln Wittig,[‡] Michel Sassi,[§] Chang-Yu Sun,[†] Matthew A. Marcus,[∥] Henrik Birkedal,[‡] Elia Beniash,[⊥] Kevin M. Rosso,[§] and Pupa U. P. A. Gilbert*[,†,#,□]

[†]Department of Physics, University of Wisconsin, Madison, Wisconsin 53706, United States
[‡]Department of Chemistry and iNANO, Aarhus University, Aarhus, 8000, Denmark
[§]Physical Sciences Division, Pacific Northwest National Laboratory, Richland, Washington 99352, United States
[∥]Advanced Light Source, Lawrence Berkeley National Laboratory, Berkeley, California 94720, United States
[⊥]Departments of Oral Biology and Bioengineering, Center for Craniofacial Regeneration, McGowan Institute for Regenerative Medicine, School of Dental Medicine, UPitt, Pittsburgh, Pennsylvania 15261, United States
[#]Departments of Chemistry, Materials Science, and Geoscience, University of Wisconsin, Madison, Wisconsin 53706, United States

Supporting Information

ABSTRACT: The recent observation in parrotfish teeth of X-ray linear dichroism motivated an in-depth investigation into this spectroscopic effect in various apatite crystals, including geologic hydroxyapatite ($Ca_5(PO_4)_3OH$), fluorapatite ($Ca_5(PO_4)_3F$), and their biogenic counterparts in human bone, mouse enamel, and in parrotfish bone, dentin, and enameloid, the equivalent of dental enamel in certain fish. These data are important because they now enable visualization of the nano- to microscale structure of apatite crystals in teeth and bone. Polarization-dependent imaging contrast (PIC) maps of lamellar bone, obtained with a new method that minimizes space-charge and charging effects, show the expected rotating apatite crystal orientations. PIC maps of mouse enamel reveal a complex arrangement of hydroxyapatite crystals perpendicular to the dentin−enamel junction, with rods arranged in a decussation pattern in inner enamel and nearly parallel to one another in outer enamel. In both inner and outer enamel crystal *c*-axes are not always aligned with the rod elongation direction.

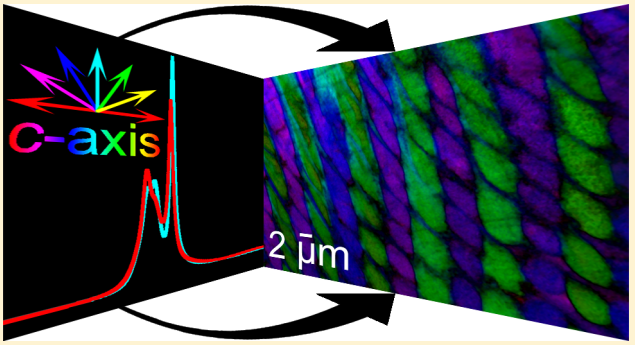

INTRODUCTION

Apatites are calcium phosphate minerals forming the main component of teeth and bone and are commonly used as fertilizer in agriculture. Despite their commanding role in biophysics, understanding the mechanical properties of this type of skeletal material remains challenging, in part because it depends on the ability to detect and unravel the hierarchical assembly patterns of biomineralized apatite polycrystals and apatite−protein composites in three dimensions.

An excellent method for measuring crystallite orientations in various materials and biominerals is based on X-ray linear dichroism,[1−3] the physical effect in which the difference in absorption of X-rays at different polarization yields an orientation-dependent signal. This effect has been used extensively for calcium carbonates.[4−13]

The existence and use of apatite X-ray linear dichroism to-date remains almost completely unexplored. Here we show that apatite is indeed dichroic, and this observation can be used not only to detect apatite crystal orientation but also to reveal the assembled orientations of crystals at the mesoscale, that is, between 10 nm and 10 μm, which is critical because the hierarchical structures of bone and teeth remain unresolved at this scale.

At the nanoscale, transmission electron microscopy reveals that bone and dentin are made of collagen interspersed with 50 nm × 25 nm × 3 nm apatite platelets.[14,15] Enamel contains crystals elongated along the *c*-axis direction,[16] ∼100 nm wide and many microns long,[17] with only sparse residual protein fragments between them.[18]

At the microscale, the elongated crystals of enamel are approximately co-oriented to one another in 5-μm-wide crystal bundles termed rods or prisms,[17−19] which arrange to form an intricate interwoven structure.[20] In long bones, the nanoscale platelets are collectively oriented at the microscale with their *c*-axes parallel (±30°)[21] to one another and to the bone long axis.

At the mesoscale, the pattern of crystal orientations in teeth and bone remains poorly known, due primarily to the lack of microscopy methods sensitive to the orientation of single crystals, which can detect the relative position and orientation of many such nanocrystals in their pristine arrangement.

Received: May 30, 2018

DOI: 10.1021/jacs.8b05547
J. Am. Chem. Soc. XXXX, XXX, XXX−XXX

The mesoscale orientation of hydroxyapatite ($Ca_5(PO_4)_3OH$, abbreviated as HAP) nanocrystals in teeth and bone is of interest not only to fundamental chemists but to materials chemists designing new materials for bone implants and to physical chemists investigating the fundamental correlations of structure and properties in natural biomaterials.[22−27]

Similarly, fluorapatite ($Ca_5(PO_4)_3F$, abbreviated as FAP) crystals form in humans when enamel surface is remineralized in the presence of fluoride, and the result is more resistant to acid than the original enamel.[28] FAP elongated crystals also form enameloid in some fish, including sharks and parrotfish. The latter bite corals with their teeth, which are extraordinarily stiff, hard, fracture-tough, and abrasion-resistant.[29] FAP is also used in the mantis shrimp club, which, tough and damage-tolerant, hits clams until their shells break.[30,31] In both cases the mesoscale arrangement of FAP crystals remains poorly understood.

Here we first analyzed single crystals of geologic HAP (Snarum, Norway) and FAP (Yates Mine, Otter Lake, Québec, Canada) by acquiring X-ray absorption near-edge structure (XANES) spectra,[32] using a photoemission electron microscope (PEEM) at the Advanced Light Source, and an elliptically polarizing undulator as the photon source. The illuminating soft-X-ray beam was linearly polarized in a variable direction over a 90° range, at the oxygen K-edge, the phosphorus $L_{2,3}$-edge, and the calcium $L_{2,3}$-edge and K-edge. We then analyzed important archetypal biological samples to fully characterize apatite dichroism, and its usefulness in analyzing and understanding the patterns of crystal orientations at the mesoscale in teeth and bone.

RESULTS AND DISCUSSION

Curiously, the P and O spectra did not show any detectable differences between polarizations parallel and perpendicular to the *c*-axis, whereas both the Ca L-edge and K-edge spectra did. Specifically, we observed that at the L-edge the intensities of two peaks vary and are anticorrelated as the linear polarization is rotated. This effect is known as X-ray linear dichroism,[1−3] and it is not *per se* surprising, as any crystal with a noncubic unit cell could in principle exhibit some dichroism. However, the magnitude of the effect, the energy positions of detectable differences, and their origins in terms of electronic structure are not easily predictable without first-principles calculations compared against direct benchmarking measurements on single crystals, as done here. This effect was previously observed in carbonate biominerals, including aragonite ($CaCO_3$) nacre[4−6] and coral skeletons,[7,8] calcite ($CaCO_3$) sea urchin teeth[10,11] and mollusc shell prisms,[12] and vaterite ($CaCO_3$) tunicate spicules.[13] However, to the best of our knowledge apatite dichroism has been previously observed only once in parrotfish teeth FAP and geologic FAP,[29] not in HAP, either geologic or biogenic, and has not been fully characterized spectroscopically nor understood theoretically, as done here. In HAP and FAP, dichroic peaks at the Ca L-edge were found at 352.6 and 351.6 eV, labeled as peaks 1 and 2 in Figure 1. Interestingly and unusually, all peaks also shift by 0.1 eV with polarization, as explained by theory below.

The FAP structure contains two symmetry-inequivalent Ca sites, as shown in the structural motifs in Figure 1, one in which two neighboring Ca atoms are at the center of irregular polyhedra that are face sharing with three common O1 atoms. In this site each Ca is surrounded by and bonded to 9 O atoms. The other site has three Ca atoms at the center of pentagonal bipyramids, which share a corner where an F atom is located. Here each Ca is bonded to 1 F and 6 O atoms and is therefore seven-coordinated. The contributions from each of these calcium sites to the Ca L_2-edge XANES spectra were investigated theoretically using the FDMNES code,[33] which

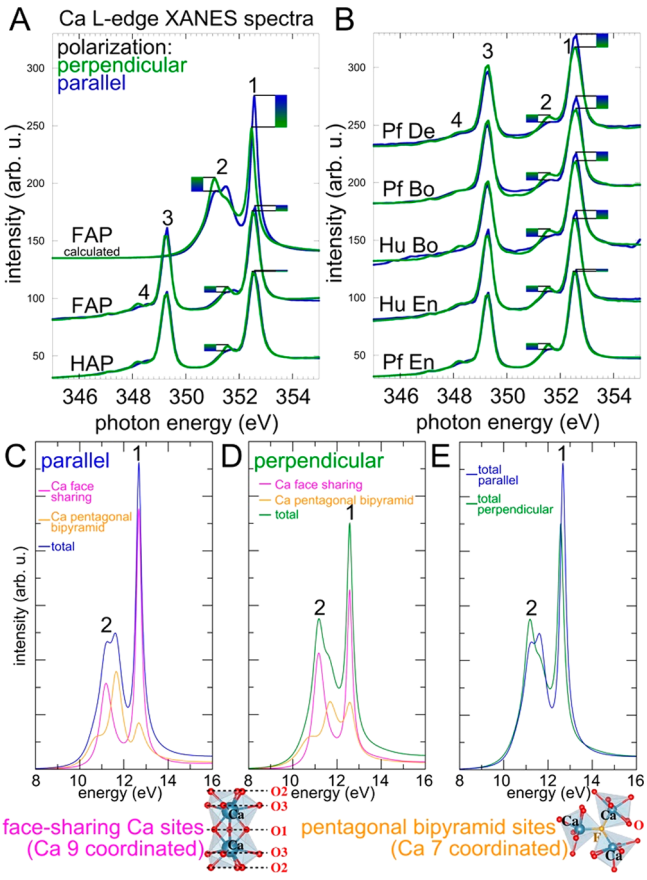

Figure 1. Experimental Ca L-edge XANES spectra of fluorapatite (FAP), hydroxyapatite (HAP), dentin (De), bone (Bo), enamel (En), or enameloid (En), from humans (Hu) or parrotfish (Pf), and calculated spectra for FAP. The mouse and human enamel spectra are identical; thus only the Hu En spectrum is shown, for clarity. Each experimental spectrum in A and B was obtained from 100 to 200 spectra extracted from 20 to 60 nm single pixels, aligned, averaged, aligned to all other spectra, normalized, and displaced vertically for clarity. (A) Macroscopic geologic apatite single crystals were mounted with a known *c*-axis orientation, and the linear polarization of the X-rays was rotated to be parallel or perpendicular to the *c*-axis, to acquire the blue or green spectra, respectively. (B) Spectra from biogenic apatite nanocrystals extracted from pixels with at least 90% parallel or perpendicular spectral line shape. All spectra exhibit X-ray linear dichroism; that is, the intensities of peaks 1 and 2 are anticorrelated. When the linear polarization is parallel or perpendicular to the *c*-axis, the peaks are maximum and minimum, respectively (see vertical green-blue gradients in A and B). Calculated Ca L_2-edge for (C) parallel and (D) perpendicular polarizations of each inequivalent Ca atom site in the FAP structure. Contributions from face-sharing and pentagonal bipyramid Ca sites are individually represented in C and D. (E) Weighted sum of calculated spectra from both sites. These same spectra are also shown in A, after shifting the energy axis ($E_{exper} = E_{calc} + 339.9$ eV) and scaling the intensity ($I_{exper} = I_{calc}/2 + 135$). Notice the excellent agreement of calculated and experimental spectral line shapes (A, peaks 1 and 2), including peak intensities, dichroism, branching ratio, and peak 2 splitting in parallel spectra (A, C, E). In addition, all peaks shift by −0.1 eV when rotating the polarization from parallel to perpendicular to the *c*-axis, in all experimental and calculated spectra.

DOI: 10.1021/jacs.8b05547
J. Am. Chem. Soc. XXXX, XXX, XXX−XXX

includes spin−orbit coupling treatment, and the FAP structure from Hughes et al.[34] and weighted according to their 6:4 stoichiometry. This analysis indicates that for parallel polarization the intensity of peak 1 is mainly due to face-sharing Ca sites, whereas the intensity of peak 2 has an almost equivalent contribution from each of the two sites. For perpendicular polarization, face-sharing sites contribute about 3× and 2× more to the intensities of peak 1 and 2, respectively, than pentagonal bipyramid sites. Similar to experimental spectra, the calculated total spectra at parallel and perpendicular polarization show anticorrelated dichroic peaks 1 and 2 and a small energy shift of all peaks by −0.1 eV.

At parallel or perpendicular polarization the spectral contributions of the two Ca sites are anticorrelated (magenta and orange peaks in Figure 1C,D). For face-sharing sites, the intensities of peaks 1 and 2 decrease and increase, respectively, when the polarization changes from parallel to perpendicular, whereas for pentagonal bipyramidal sites, they increase and decrease, respectively. For face-sharing Ca sites, peak 1 has contributions from all of the Ca−O bonds, whereas peak 2 has contributions mainly from the Ca−O3 bonds. The small energy shift observed can be explained by analyzing the relative energy of the orbitals probed. A detailed analysis of the electron density revealed that peak 1 has major contributions from calcium d_{yz} and d_{xz} orbitals, probed with both parallel and perpendicular polarizations, whereas peak 2 has contribution from either the d_{z^2} orbital or d_{xy} and $d_{x^2-y^2}$ orbitals when probed with parallel or perpendicular polarization, respectively. Because the energy of the d_{xy} and $d_{x^2-y^2}$ orbitals is 0.1 eV lower than for the d_{z^2} orbital, all peaks are shifted by −0.1 eV for perpendicular compared to parallel polarizations, in agreement with the experimental spectra at the peak 1 energy position. In the case of pentagonal bipyramid sites, each of the two peaks has a mixed contribution from all the Ca−O and Ca−F bonds.

The agreement of experimental and calculated FAP spectra in Figure 1A is remarkable, especially considering that these calculations are *ab initio*, without any parameters empirically adjusted to match the experiments.

The observed dichroism is strongest in calculated FAP spectra (Figure 1A,E), strong in the biogenic nanocrystals of dentin and bone, weaker in enamel and enameloid (Figure 1B), and weakest in the geologic macrocrystals (Figure 1A). The lower dichroism in experimental vs calculated spectra can simply be explained by greater disorder in natural samples, and thus peak broadening in the experimental spectra.

Surprisingly, the dichroism in Figure 1 is stronger in dentin and bone (whether human, mouse, or parrotfish) than in HAP. This increase may be due to two separate effects: a surface reconstruction in bone and dentin's 3 nm thick nanocrystalline platelets and/or the surface of the platelets simply truncates the crystal structure and thus increases its anisotropy. In the larger, 100 nm thick crystals of enamel or enameloid the observed extent of dichroism is comparable to that in macro-FAP, thus corroborating the size-dependent interpretation.

Carbonated HAP, termed CHAP, dahllite, or collophane, is the mineral found in human and mouse bone, dentin, and enamel and presumably in parrotfish bone and dentin. Macroscopic single crystals of CHAP are not readily available. However, since HAP and FAP spectra are nearly identical and show similar peak 1 and 2 dichroism and because apatite is an ionic crystal in which the precise atomic composition affects bonds less than atomic charge, it is reasonable to assume that CHAP would have nearly identical spectra to HAP and FAP.

In Figure 2 we present FAP experimental and simulated spectra at the Ca K-edge. At parallel polarization, Figure 2A

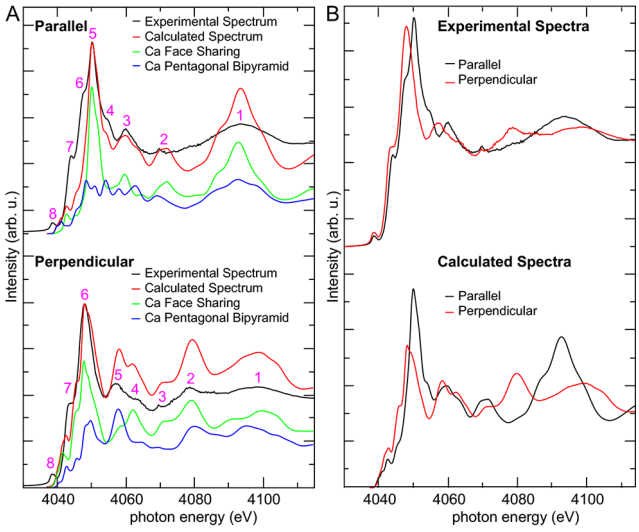

Figure 2. (A) Comparison of experimental and calculated Ca K-edge spectra, with contributions from each Ca site shown separately. (B) Comparison of the linear dichroism observed experimentally and in calculated spectra.

shows that the linear combination of the spectra calculated for face-sharing sites and pentagonal bipyramid sites reproduces the overall features of the experimental Ca K-edge spectra, despite some irregularities in the relative peak intensities and the absence of the shoulder marked 6. At perpendicular polarization, every peak of the experimental spectra could be reproduced by the linear combination of the two Ca component spectra. In addition, most of the peaks at perpendicular polarization have a dominant contribution from face-sharing Ca sites, and only peak 5 shows a major contribution from pentagonal bipyramid sites.

A side-by-side comparison of the experimental and calculated dichroism at parallel and perpendicular polarizations is shown in Figure 2B. The intensity variations and energy shifts for each peak are qualitatively reproduced by the calculations. Particularly, the energy shift of the main peak at parallel and perpendicular polarizations was calculated to be −1.9 eV, which is in very good agreement with the experimental −2.0 eV value. These larger K-edge (−2.0 eV) and the smaller L-edge (−0.1 eV) angle-dependent peak shifts associated with dichroism were unexpected, but they are not unique to apatite: they have been previously seen in Ni magnetic materials, although in the Ni^{2+} systems it is the magnetic structure that generates dichroism, not the crystal structure or orientation.[35,36]

Having learned from the spectra in Figure 1 the energies at which one must search for dichroism, we analyzed human bone, which is composed of nanocrystalline HAP or CHAP,[37−39] and mouse enamel, which is composed of HAP.[18] The results are presented in Figures 3 and 4.

The existence of measurable dichroism in apatite made it possible to acquire polarization-dependent imaging contrast (PIC) maps as was previously done with calcium carbonate biominerals.[4−9] To acquire a PIC map, we take a series of images with differing linear polarization angles and solve for the crystal orientation in each 60 nm pixel, assuming a Malus-law dependence of intensity on the angle between the polarization and the *c*-axis.[40]

DOI: 10.1021/jacs.8b05547
J. Am. Chem. Soc. XXXX, XXX, XXX−XXX

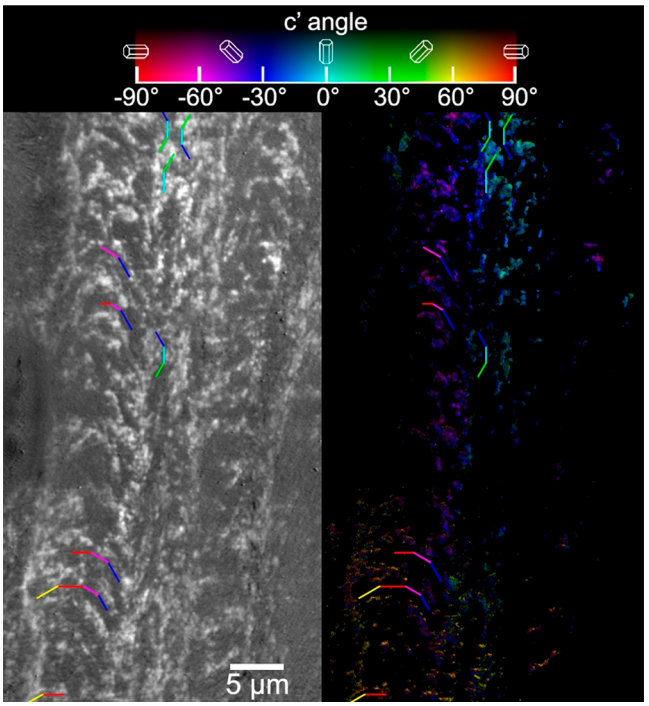

Figure 3. PEEM images of a portion of lamellar bone from a human femur. (A) Ca distribution map showing the undulating nature of lamellar bone. Notice that the distribution of calcium is uneven, as bone is not fully mineralized. (B) PIC map of the same area of bone showing individual, 57 nm pixels and their crystal orientations displayed in colors, as shown in the color legend above. To help in interpreting this PIC map, we have drawn nine arches comprising colored segments with the accurate color and angular orientation of the crystal *c*-axes, so they resemble the nearby lamellar unit. The length of each segment is arbitrarily assigned, to best assemble an arc in each lamellar unit. Additional data acquired in this and a nearby area are presented in Figures S1 and S2; the positions of both areas in the bone sample are shown in Figure S3.

For this purpose, in Figures 3 and 4 we exploited the observation in Figure 1 that the peak positions vary by 0.1 eV and that imaging contrast in PEEM images is inverted when changing photon energy from +0.2 eV above the peak 1 position to −0.2 eV below it. Thus, at each polarization (0−90°, 5° steps) we acquired PEEM images at these two energies, 352.8 and 352.4 eV, and calculated their image ratio, which greatly maximizes the contrast between differently oriented crystals. We then stacked all 19 image ratios and solved for the crystal *c*-axis orientation in each of 10^6 pixels.

The previous method used in parrotfish enameloid[29] exploited the observation in Figure 1 that the peak intensities at peaks 1 and 2 are anticorrelated, thus at each polarization images at 352.6 and 351.6 eV were acquired and their ratios calculated; they were then stacked, and each pixel's *c*-axis orientation was found as above. These two methods of obtaining a PIC map are completely equivalent and provide similar results in heavily mineralized enamel and enameloid. They are not, however, equivalent in the much less mineralized bone and dentin tissues, which exhibit strong charging effects in PEEM images; thus the images on two peaks with different intensities, as peaks 1 and 2 are, may appear with different magnifications due to charging or differently blurred due to space charge, making it impossible to calculate their ratio. The ±0.2 eV method instead, being above and below the symmetric peak 1 by identical amounts, results in identical intensities and thus no image blurring due to space charge effects[41−43] or charging-induced magnification changes,[44] as done in Figure 3. In Figure 3 the Ca distribution map was used to filter out much noise that appeared in the PIC map and was masked out by only retaining the pixels in which the Ca concentration was greater than a threshold value as described in the Supporting Information.

Figures S1 and S2 show additional data from the same area of Figure 3 and another nearby area, respectively. Where in the bone sample these data were collected is shown in Figure S3. Two more areas were analyzed in a second bone sample and are shown in Figures S4 and S5, and their positions in Figure S6. From the results of Figure 3 we conclude that the *c*-axes of bone platelets are oriented along the lamellar unit arc. This result was expected, as Weiner et al. already observed in 1997 that bone fibrils rotate within a lamellar unit in 30° increments and termed this the plywood structure.[21,45] Later it became known as the Bouligand structure of lamellar bone.[46] The results of bone PIC mapping in Figure 3 are discontinuous in space, but where crystal orientations are detectable, they confirm the Bouligand structure and thus serve to validate the PIC mapping method in bone.

In Figure 4 we present the PIC map of a mouse incisor tooth. The inner enamel near the dentin enamel junction (DEJ) shows a blue layer a few micrometers thick. The blue hues of this layer indicate that *c*-axes of the crystals in this layer are oriented normally to the DEJ (see inset) as was previously shown.[47]

The bulk of the inner enamel consists of interdigitating bundles of crystals termed rods or prisms, at different angles with respect to the DEJ and organized in alternating groups at a 60−70° angle from each other.[48] This arrangement is termed decussation pattern, and it is magnified in an inset in Figure 4.

In the decussation pattern blue and green crystals are oriented 60° from one another, which is approximately consistent with Cox's previous observation that rods run 70° from one another in space.[48] Importantly, however, in the inner enamel *c*-axes of the crystals are not aligned with the rod axes, as previously postulated. Specifically, this is evident in the green rods in the decussation pattern inset, which have elliptical cross sections, as opposed to circular, with the ellipses elongated along the direction in which the rods run. This direction is approximately −30°; thus if the assumption that crystal *c*-axes and rods run in the same direction were correct, the crystal orientation would be −30°, but it is not. It is in fact +30° (green). This observation is inconsistent with coalignment of *c*-axes and rod axes in inner enamel.

It has been the subject of a long-standing debate whether or not mouse enamel contains inter-rod crystals. The PIC map in Figure 4 shows magenta crystals between blue rods and cyan crystals between green rods, which may play a crack deflection role similar to the inter-rod in human enamel.[49]

As they approach the outer enamel, the rods sharply change their directions, and they kink, to align almost parallel to the enamel surface.[50] Interestingly, many prisms that were blue before the kink become green after the kink, which is a ∼60° orientation change, whereas their morphological directions kink by more than 90°. Surprisingly, after kinking, the yellow and orange hues expected from observing the prism elongation direction in the PIC map never appear. Thus, in outer enamel, as described above in inner enamel, crystallographic orientation does not necessarily follow the rod elongation direction.

Furthermore, it has been long assumed that the crystals in a rod are co-oriented with the rod long axis.[51,52] In Figure 4,

DOI: 10.1021/jacs.8b05547
J. Am. Chem. Soc. XXXX, XXX, XXX−XXX

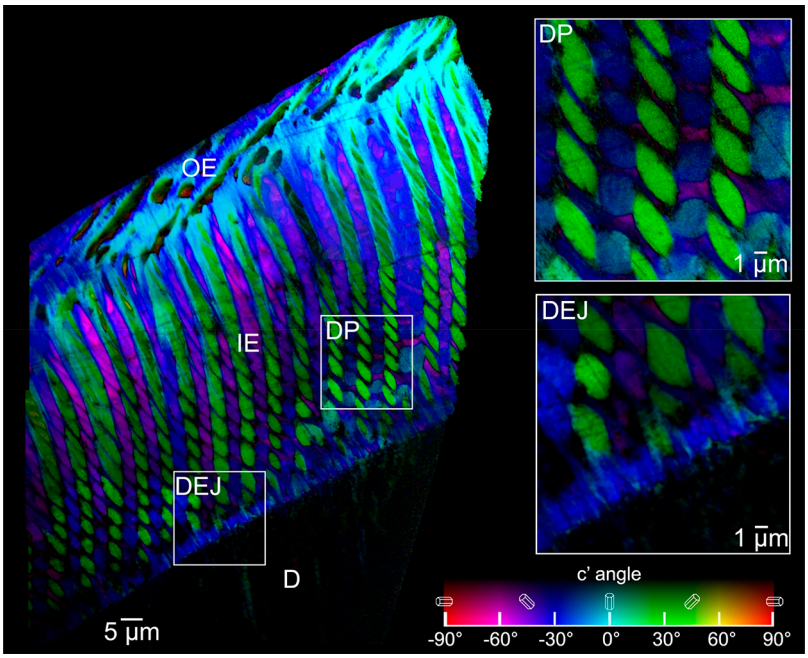

Figure 4. PIC map of a mouse incisor midsagittal polished cross-section. Bottom to top one can see at the tooth interior the dentin (D) layer, which appears darker, as it is less mineralized, the dentin−enamel junction (DEJ) line, the inner enamel (IE) and outer enamel (OE) layers, and the biting tip at top right. Notice that both IE and OE contain bundles of nearly co-oriented crystals, termed prisms or rods, which in the IE interdigitate to form a decussation pattern (DP). The white boxes indicate the regions magnified in the correspondingly labeled insets on the right, acquired with 20 and 60 nm pixels, in DP and DEJ, respectively.

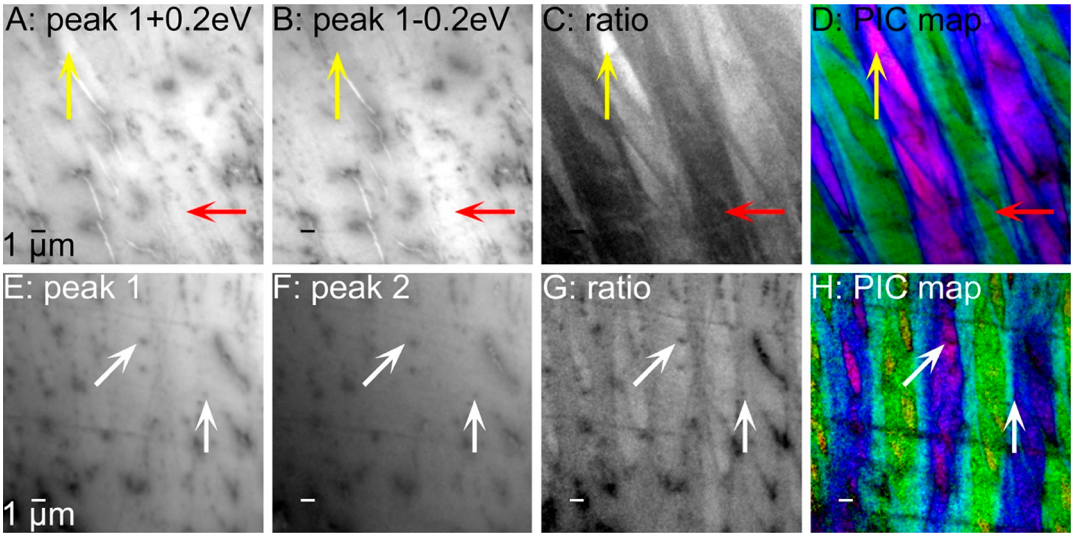

Figure 5. Charging artifacts in PEEM images, which affect PIC map quality. Panels A−D were acquired or calculated from the same region; so are E−H, from a different region of mouse enamel. (A, B) Single PEEM images acquired 0.2 eV above and below the peak 1 energy, respectively, with horizontal (0°) polarization. These images were separately leveled in Photoshop for visibility in this figure; thus brightness should not be compared here. The original images do not vary much in intensity, but they do vary in contrast, depending on crystal orientation. For example, compare the enamel rod indicated by the yellow arrow, which is brighter in A and darker in B, or the one indicated by the red arrow, which does the opposite. (C) Digital ratio of the two images in A and B. (D) PIC map calculated from 19 image ratios like one in C, repeated at each polarization from 0° to 90°, and stacked. The energies in A and B yield the best PIC map and minimize charging effects. (E, F) Single PEEM images acquired at peak 1 and peak 2 energies, respectively. Again, these were acquired with 0° polarization and were leveled separately for visibility. E and F images differ in intensity dramatically, which introduces blurring, interpreted as space-charge. The two white arrows indicate features sharp at peak 1, where the image was focused, which become blurred at peak 2. Other features in this image also blur at peak 2. (G) Digital ratio of images in E and F. Due to blurring in F, all features imperfectly correspond spatially between E and F; thus the ratio image in G is blurred and noisy. (H) PIC map calculated for this area, which is inevitably blurred and noisy. Compare the two PIC maps here (D and H) to see the difference in quality and the superiority of using peak 1 ± 0.2 eV energies for PIC mapping.

despite all rods in the outer enamel elongating nearly parallel to one another, many orientations can be distinguished in the PIC map: elongated green, dark green, or black rods, the latter indicating *c*-axes oriented out of the image plane, are surrounded

DOI: 10.1021/jacs.8b05547
J. Am. Chem. Soc. XXXX, XXX, XXX−XXX

by blue and cyan crystals; thus angle spreads as large as 60° are observed in the outer enamel. These results change significantly our understanding of the crystallographic organization of mouse enamel.

Notice in Figures 3 and 4 that many orientations (colors) are present, in beautifully intertwined crystal arrangements in bone and enamel. Subdivision into multiple structural components in a biomineral is a well-known toughening mechanism.[53] Most biominerals, however, have nearly co-oriented crystals, as in nacre tablets[6] or tunicate spicules,[13] or perfectly co-oriented crystals as in sea urchin spines.[54] In human bone and mouse enamel the complex arrangement of crystal morphologies and the multiple orientations observed here may contribute to provide these vital biominerals with their functions.

We note that enamel provides higher quality PIC maps than bone and dentin, as easily seen by a comparison of Figures 3 and 4. This is because enamel is more heavily mineralized, polishes more homogeneously, and is less porous than bone and dentin, all of which contribute to lower charging effects in enamel. See Figure 5 for an illustration of charging artifacts in PEEM experiments, which affect PIC mapping and prevent a quantitative assessment of dichroism in different biominerals. The more mineralized and space-filling[8,55] a biomineral is, the better for PIC mapping. Even for enamel, obtaining the PIC map by exploiting the small shift that peak 1 shows with polarization dramatically improves the quality of PIC maps, as shown in Figure 5.

CONCLUSIONS

We have demonstrated and exploited X-ray linear dichroism for visualizing the mesoscale structure of apatites assembled in some archetypal biomineralized structures in two dimensions, with *c*-axis orientations in three dimensions. Comparison of measured and calculated dichroism on single crystals shows excellent correspondence. These spectra and the new approach to PIC mapping to minimize charging artifacts in human bone and mouse enamel, combined, establish the feasibility of mapping and understanding the orientations of HAP and FAP nano- and microcrystals and their structural arrangement in complex, hierarchical skeletal materials such as human bone and mouse enamel. This technique enables a host of future studies on important topics, including comparison of healthy and unhealthy bone[56] and teeth.[57] For now, it has helped reveal in exquisite detail the precise structure of mouse enamel.

ASSOCIATED CONTENT

Supporting Information

The Supporting Information is available free of charge on the ACS Publications website at DOI: 10.1021/jacs.8b05547.

Figures S1−S6, detailed methods, sample preparation, overabsorption in K-edge spectra, SEM analysis, Ca spectroscopy, PIC mapping, masking of bone PIC maps, FDMNES calculated spectra, supporting references (PDF)

AUTHOR INFORMATION

Corresponding Author

*pupa@physics.wisc.edu

ORCID

Michel Sassi: 0000-0003-2582-3735

Henrik Birkedal: 0000-0002-4201-2179

Elia Beniash: 0000-0001-9019-5160

Kevin M. Rosso: 0000-0002-8474-7720

Pupa U. P. A. Gilbert: 0000-0002-0139-2099

Notes

The authors declare no competing financial interest.

□Previously publishing as Gelsomina De Stasio.

ACKNOWLEDGMENTS

We thank Andreas Scholl for technical support and Hajime Yamazaki and Henry Margolis for providing the mouse tooth sample. P.G. acknowledges support from the U.S. Department of Energy (DOE), Office of Science, Office of Basic Energy Sciences (OBES), Chemical Sciences, Geosciences, and Biosciences Division (CSGB), under Award DE-FG02-07ER15899, NSF grant DMR-1603192. K.M.R. and M.S. acknowledge support from the DOE OBES CSGB Division through its Geosciences program at Pacific Northwest National Laboratory (PNNL). H.B. and N.K.W. acknowledge affiliation with the Center for Integrated Materials Research (iMAT) at Aarhus University, the Danish Agency for Science, Technology, and Innovation for funding (DANSCATT), and the Villum Fonden grant 17553. All data were acquired at the Advanced Light Source, Lawrence Berkeley National Laboratory, supported by the Director, Office of Science, OBES, DOE, under contract number DE-AC02-05CH11231. PNNL is a multiprogram national laboratory operated for the DOE by Battelle.

REFERENCES

(1) Stöhr, J.; Baberschke, K.; Jaeger, R.; Treichler, R.; Brennan, S. *Phys. Rev. Lett.* **1981**, *47*, 381.

(2) Ade, H.; Hsiao, B. *Science* **1993**, *262*, 1427.

(3) Stöhr, J.; Scholl, A.; Regan, T. J.; Anders, S.; Lüning, J.; Scheinfein, M. R.; Padmore, H. A.; White, R. L. *Phys. Rev. Lett.* **1999**, *83*, 1862.

(4) Metzler, R. A.; Abrecht, M.; Olabisi, R. M.; Ariosa, D.; Johnson, C. J.; Frazer, B. H.; Coppersmith, S. N.; Gilbert, P. U. P. A. *Phys. Rev. Lett.* **2007**, *98*, 268102.

(5) Metzler, R. A.; Zhou, D.; Abrecht, M.; Chiou, J.-W.; Guo, J.; Ariosa, D.; Coppersmith, S. N.; Gilbert, P. U. P. A. *Phys. Rev. B: Condens. Matter Mater. Phys.* **2008**, *77*, 064110.

(6) Gilbert, P. U. P. A.; Bergmann, K. D.; Myers, C. E.; Marcus, M. A.; DeVol, R. T.; Sun, C.-Y.; Blonsky, A. Z.; Tamre, E.; Zhao, J.; Karan, E. A.; Tamura, N.; Lemer, S.; Giuffre, A. J.; Giribet, G.; Eiler, J. M.; Knoll, A. H. *Earth Planet. Sci. Lett.* **2017**, *460*, 281.

(7) DeVol, R. T.; Sun, C.-Y.; Marcus, M. A.; Coppersmith, S. N.; Myneni, S. C. B.; Gilbert, P. U. P. A. *J. Am. Chem. Soc.* **2015**, *137*, 13325.

(8) Mass, T.; Giuffre, A. J.; Sun, C.-Y.; Stifler, C. A.; Frazier, M. J.; Neder, M.; Tamura, N.; Stan, C. V.; Marcus, M. A.; Gilbert, P. U. P. A. *Proc. Natl. Acad. Sci. U. S. A.* **2017**, *114*, E7670.

(9) Gilbert, P. U. P. A. *Microsc. Microanal.* **2018**, *24*, 454.

(10) Ma, Y. R.; Aichmayer, B.; Paris, O.; Fratzl, P.; Meibom, A.; Metzler, R. A.; Politi, Y.; Addadi, L.; Gilbert, P. U. P. A.; Weiner, S. *Proc. Natl. Acad. Sci. U. S. A.* **2009**, *106*, 6048.

(11) Killian, C. E.; Metzler, R. A.; Gong, Y. U. T.; Churchill, T. H.; Olson, I. C.; Trubetskoy, V.; Christensen, M. B.; Fournelle, J. H.; De Carlo, F.; Cohen, S.; Mahamid, J.; Wilt, F. H.; Scholl, A.; Young, A.; Doran, A.; Coppersmith, S. N.; Gilbert, P. U. P. A. *Adv. Funct. Mater.* **2011**, *21*, 682.

(12) Gilbert, P. U. P. A.; Young, A.; Coppersmith, S. N. *Proc. Natl. Acad. Sci. U. S. A.* **2011**, *108*, 11350.

(13) Pokroy, B.; Kabalah-Amitai, L.; Polishchuk, I.; DeVol, R. T.; Blonsky, A. Z.; Sun, C.-Y.; Marcus, M. A.; Scholl, A.; Gilbert, P. U. P. A. *Chem. Mater.* **2015**, *27*, 6516.

(14) Weiner, S.; Wagner, H. D. *Annu. Rev. Mater. Sci.* **1998**, *28*, 271.

DOI: 10.1021/jacs.8b05547
J. Am. Chem. Soc. XXXX, XXX, XXX−XXX

(15) Wegst, U. G.; Bai, H.; Saiz, E.; Tomsia, A. P.; Ritchie, R. O. *Nat. Mater.* **2015**, *14*, 23.
(16) Selvig, K. A. *J. Ultrastruct. Res.* **1972**, *41*, 369.
(17) Habelitz, S.; Marshall, S.; Marshall, G.; Balooch, M. *Arch. Oral Biol.* **2001**, *46*, 173.
(18) Ten Cate, A. R. *Oral Histology: Development, Structure, and Function*, 4th ed.; Mosby: Toronto, 1994.
(19) Fang, P.-A.; Conway, J. F.; Margolis, H. C.; Simmer, J. P.; Beniash, E. *Proc. Natl. Acad. Sci. U. S. A.* **2011**, *108*, 14097.
(20) Lowenstam, H. A.; Weiner, S. *On Biomineralization*; Oxford University Press: New York, 1989.
(21) Weiner, S.; Arad, T.; Sabanay, I.; Traub, W. *Bone* **1997**, *20*, 509.
(22) Gunaratne, G. H.; Rajapaksa, C. S.; Bassler, K. E.; Mohanty, K. K.; Wimalawansa, S. J. *Phys. Rev. Lett.* **2002**, *88*, 068101.
(23) Gupta, H. S.; Messmer, P.; Roschger, P.; Bernstorff, S.; Klaushofer, K.; Fratzl, P. *Phys. Rev. Lett.* **2004**, *93*, 158101.
(24) Weinkamer, R.; Hartmann, M. A.; Brechet, Y.; Fratzl, P. *Phys. Rev. Lett.* **2004**, *93*, 228102.
(25) Rusconi, M.; Zaikin, A.; Marwan, N.; Kurths, J. *Phys. Rev. Lett.* **2008**, *100*, 128101.
(26) Li, Y.; Ortiz, C.; Boyce, M. C. *Phys. Rev. E* **2011**, *84*, 062904.
(27) Najman, M. N.; Kasrai, M.; Bancroft, G. M.; Frazer, B. H.; De Stasio, G. *Tribol. Lett.* **2004**, *17*, 811.
(28) Selwitz, R. H.; Ismail, A. I.; Pitts, N. B. *Lancet* **2007**, *369*, 51.
(29) Marcus, M. A.; Amini, S.; Stifler, C. A.; Sun, C.-Y.; Frazier, M. J.; Tamura, N.; Bechtel, H. A.; Parkinson, D. Y.; Barnard, H. S.; Zhang, X. X. X.; Chua, J. Q. I.; Miserez, A.; Gilbert, P. U. P. A. *ACS Nano* **2017**, *11*, 11856.
(30) Weaver, J. C.; Milliron, G. W.; Miserez, A.; Evans-Lutterodt, K.; Herrera, S.; Gallana, I.; Mershon, M. J.; Swanson, B.; Zavattieri, P.; DiMasi, E.; Kisailus, D. *Science* **2012**, *336*, 1275.
(31) Tadayon, M.; Amini, S.; Masic, A.; Miserez, A. *Adv. Funct. Mater.* **2015**, *25*, 6437.
(32) Stöhr, J. *NEXAFS Spectroscopy*; Springer-Verlag: Berlin, 1992; Vol. *25*.
(33) Bunău, O.; Joly, Y. *J. Phys.: Condens. Matter* **2009**, *21*, 345501.
(34) Hughes, J. M.; Cameron, M.; Crowley, K. D. *Am. Mineral.* **1989**, *74*, 870.
(35) Arenholz, E.; van der Laan, G.; Chopdekar, R. V.; Suzuki, Y. *Phys. Rev. Lett.* **2007**, *98*, 197201.
(36) Wu, Y. Z.; Zhao, Y.; Arenholz, E.; Young, A. T.; Sinkovic, B.; Won, C.; Qiu, Z. Q. *Phys. Rev. B: Condens. Matter Mater. Phys.* **2008**, *78*, 064413.
(37) Boskey, A. L. *Elements* **2007**, *3*, 385.
(38) Ruppel, M.; Miller, L.; Burr, D. *Osteoporosis Int.* **2008**, *19*, 1251.
(39) Xie, B.; Nancollas, G. H. *Proc. Natl. Acad. Sci. U. S. A.* **2010**, *107*, 22369.
(40) GG−Macros http://home.physics.wisc.edu/gilbert/software.htm, 2018.
(41) Buckanie, N.; Göhre, J.; Zhou, P.; Von der Linde, D.; Horn-von Hoegen, M.; Zu Heringdorf, F. M. *J. Phys.: Condens. Matter* **2009**, *21*, 314003.
(42) Locatelli, A.; Menteş, T. O.; Niño, M. Á.; Bauer, E. *Ultramicroscopy* **2011**, *111*, 1447.
(43) Massey, G. *IEEE J. Quantum Electron.* **1983**, *19*, 873.
(44) Egerton, R.; Li, P.; Malac, M. *Micron* **2004**, *35*, 399.
(45) Weiner, S.; Traub, W.; Wagner, H. D. *J. Struct. Biol.* **1999**, *126*, 241.
(46) Bouligand, Y. *Tissue Cell* **1972**, *4*, 189.
(47) Fang, P.-A.; Lam, R. S. K.; Beniash, E. *Eur. J. Oral Sci.* **2011**, *119*, 120.
(48) Cox, B. N. *J. R. Soc., Interface* **2013**, *10*, 1.
(49) Bajaj, D.; Arola, D. *Biomaterials* **2009**, *30*, 4037.
(50) Warshawsky, H.; Smith, C. E. *Anat. Rec.* **1971**, *169*, 585.
(51) Jodaikin, A.; Weiner, S.; Traub, W. *J. Ultrastruct. Res.* **1984**, *89*, 324.
(52) Nylen, M. U.; Eanes, E. D.; Omnell, K.-Å. *J. Cell Biol.* **1963**, *18*, 109.
(53) Gao, H.; Ji, B.; Jäger, I. L.; Arzt, E.; Fratzl, P. *Proc. Natl. Acad. Sci. U. S. A.* **2003**, *100*, 5597.
(54) Moureaux, C.; Perez-Huerta, A.; Compère, P.; Zhu, W.; Leloup, T.; Cusack, M.; Dubois, P. *J. Struct. Biol.* **2010**, *170*, 41.
(55) Yang, L.; Killian, C. E.; Kunz, M.; Tamura, N.; Gilbert, P. U. P. A. *Nanoscale* **2011**, *3*, 603.
(56) Ferraz, M.; Monteiro, F.; Manuel, C. *J. Appl. Biomater. Biomech.* **2004**, *2*, 74.
(57) Beniash, E.; Simmer, J. P.; Margolis, H. C. *J. Struct. Biol.* **2005**, *149*, 182.

DOI: 10.1021/jacs.8b05547
J. Am. Chem. Soc. XXXX, XXX, XXX−XXX

Supporting Information
for

X-ray linear dichroism in apatite

Cayla A. Stifler[a], Nina Kølln Wittig[b], Michel Sassi[c], Chang-Yu Sun[a], Matthew A. Marcus[d], Henrik Birkedal[b], Elia Beniash[e], Kevin M. Rosso[c], and Pupa U. P. A. Gilbert[a,f,*]

[a] University of Wisconsin–Madison, Department of Physics, Madison WI 53706 USA.
[b] Aarhus University, Department of Chemistry and iNANO, Aarhus, 8000, Denmark.
[c] Physical Sciences Division, Pacific Northwest National Laboratory, Richland, WA, 99352, USA.
[d] Advanced Light Source, Lawrence Berkeley National Laboratory, Berkeley, CA, 94720, USA.
[e] Departments of Oral Biology and Bioengineering, Center for Craniofacial Regeneration, McGowan Institute for Regenerative Medicine, School of Dental Medicine, UPitt, Pittsburgh, PA 15261, USA.
[f] University of Wisconsin–Madison, Departments of Chemistry, Materials Science, and Geoscience, Madison WI 53706 USA.

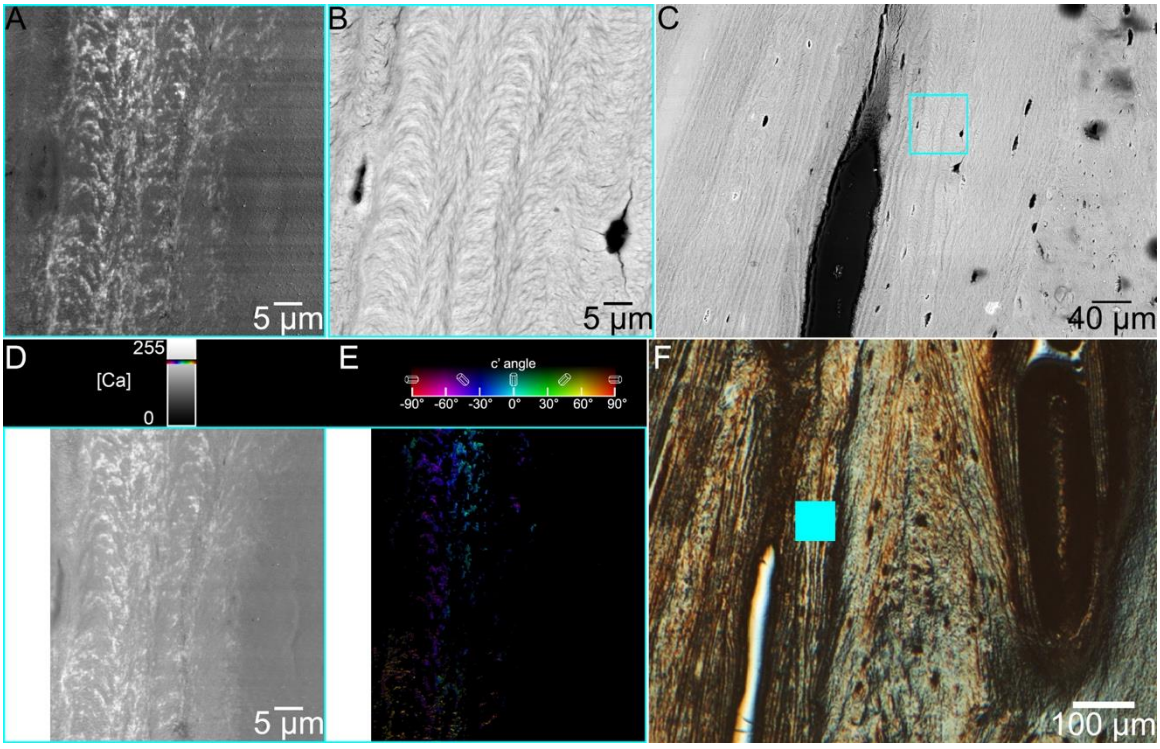

Figure S1. Spectromicroscopy of lamellar bone with curved Bouligand lines clearly visible. A. Average of 19 PEEM images acquired at different polarizations, in which the crystal orientation information is minimized, and the brightness is proportional to Ca density. B. SEM image of the same area, at identical magnification. C. SEM image at lower magnification, where the area in A, B, and in Figure 3 is outlined in cyan. D. Ca distribution map obtained by ratio of images acquired on- and off-peak 1 using PEEM. The Ca map in Figure 3 is contrast enhanced in Photoshop. This one is not, so the [Ca] is quantitatively measured, and displayed as grayscale according to the gradient legend on top, with 0 (black) corresponding to no Ca and high Ca concentration corresponding to 255 (white). This quantitative measurement is not calibrated. The rainbow bar in the [Ca] scale is placed at 190. E. PIC map as in Figure 3, indicating crystal orientations quantitatively in color. A threshold at graylevel 190 of the Ca map in D was used to mask off the noise in all pixels with low Ca concentration. F. Visible light microscopy (VLM) image, obtained by differential interference contrast (DIC)[1] in reflection mode, where the source of contrast is mostly topography of the polished bone sample surface. The region analyzed in Figure 3 and in panels A, B, D, E here is shown as a cyan square. The maps in D and E were cropped on the left to eliminate image alignment artifacts, which is why the cyan outlines in D and E include a blank region on the left.

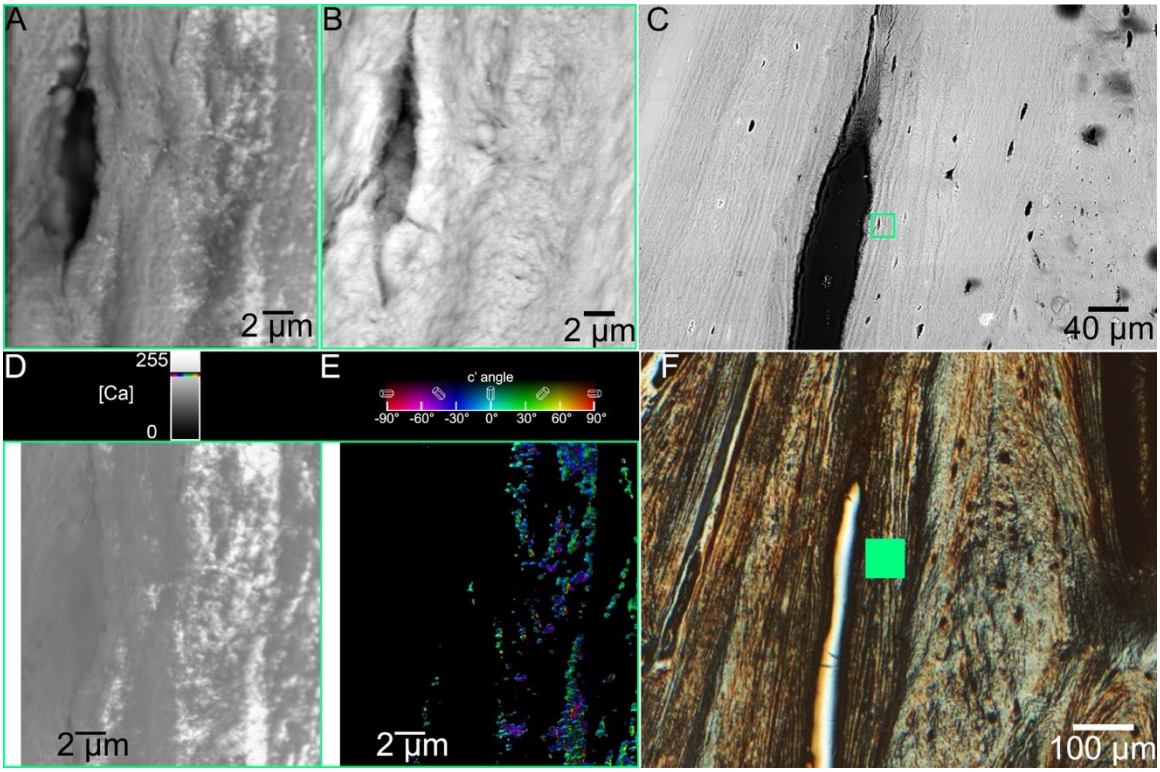

Figure S2. Spectromicroscopy of lamellar bone with no discernible Bouligand structure. All panels are organized and obtained precisely as in Figure S2, with the relevant region outlined in green here, and the PIC map masked with a Ca map thresholded at graylevel 190 again.

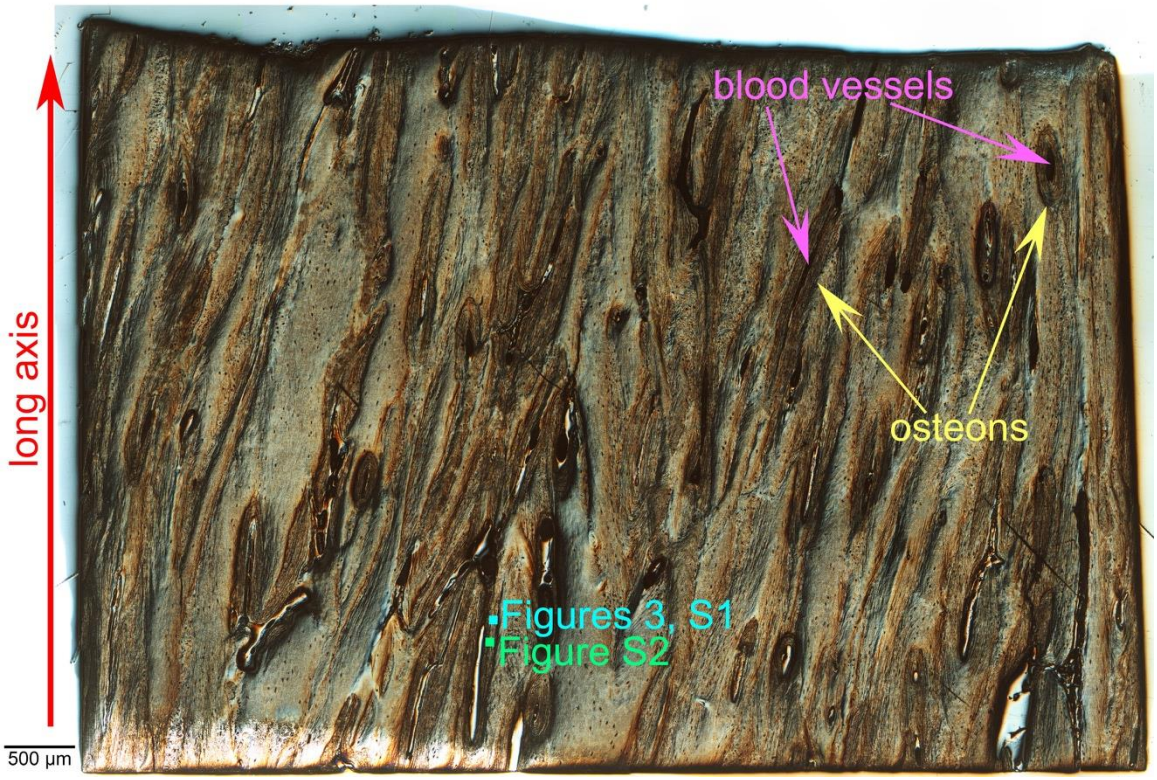

Figure S3. Human bone cut along the bone long axis, embedded, polished, and coated for PEEM analysis and PIC mapping. Many osteons are visible in this section, with concentric rings of lamellar bone structures (yellow arrows), each surrounding a blood vessel (pink arrows). Many blood vessels and osteons run parallel to the bone long axis, vertical in this section, and some run nearly perpendicular to it. The arrows show two extreme cases, in which the osteons appear elongated or elliptical, respectively. Two light blue and light green squares indicate the precise positions in which the PIC maps in Figures 3, S1 and S2 were acquired.

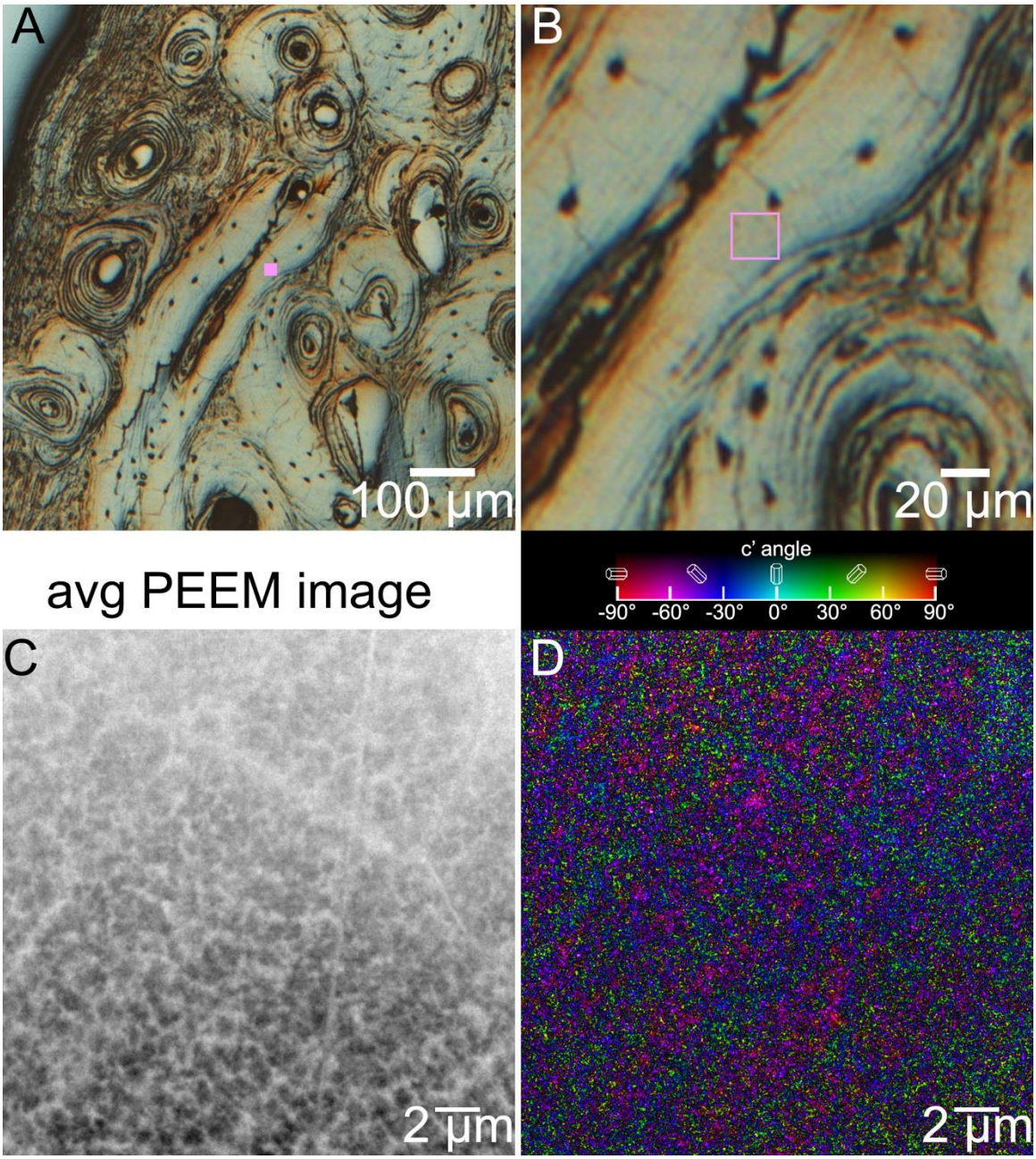

Figure S4. Lamellar bone from an osteon with the central blood vessel running in-plane on the sample surface. A. VLM-DIC image showing the area of interest as a pink square. B. Zoomed in VLM-DIC image showing the area as a pink box. C. Average image of PEEM stack, acquired in the pink region indicated in A and B. D. PIC map obtained from the same region in A, B, C, with the same data acquisition and processing used for Figures 3, S1, S2, but without any masks, thus the noisy low-Ca regions of bone remain exposed. Nevertheless, a band along the diagonal from bottom left to top right, and other striations parallel to the diagonal remain visible. These are characteristic of lamellar bone.

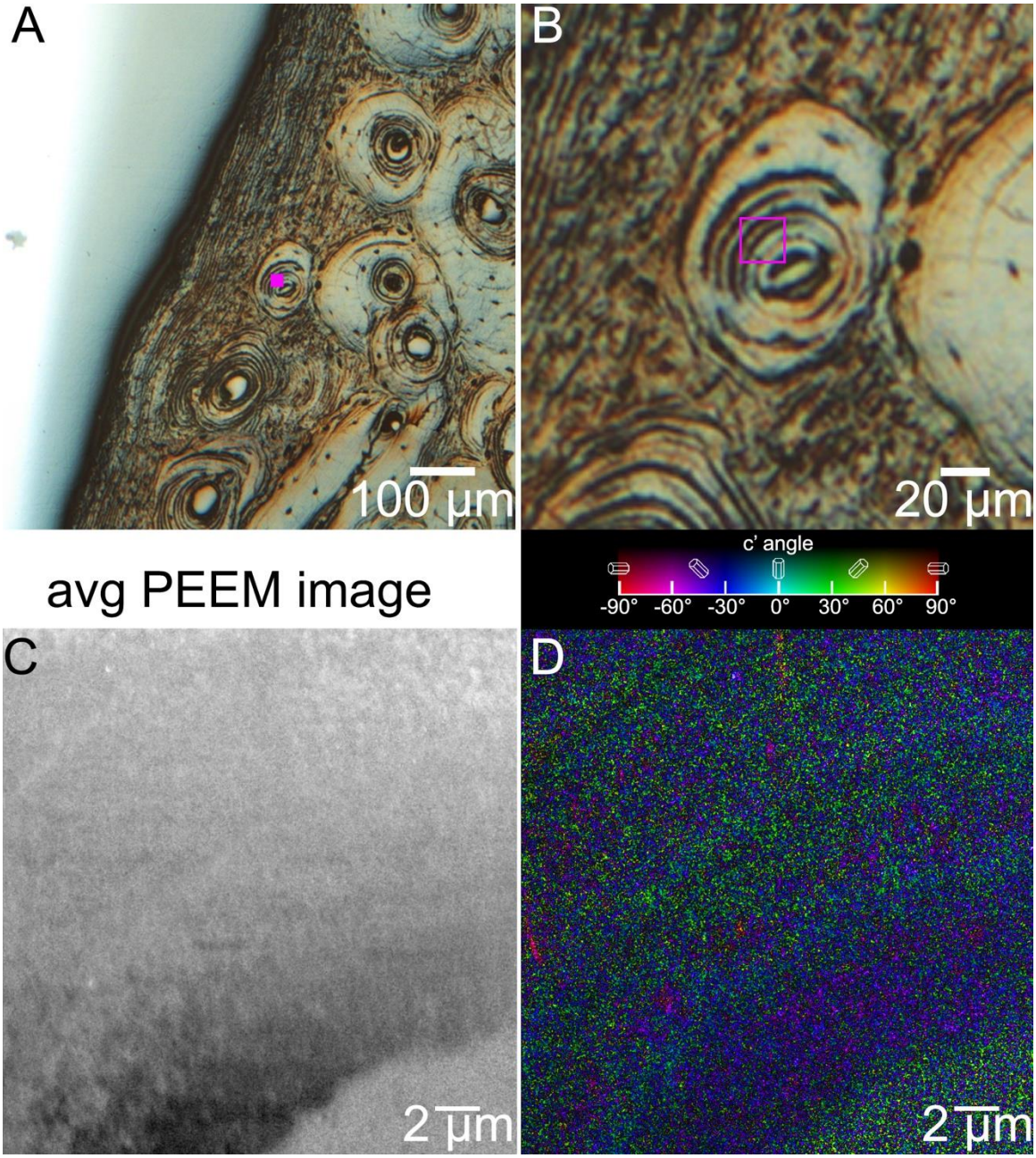

Figure S5. Lamellar bone from an osteon with the central blood vessel perpendicular to the sample surface. All panels are presented as in Figure S4, with the magenta region in A and B magnified in C and D. The PIC map in D shows faint concentric rings surrounding the blood vessel, which are also characteristic of lamellar bone.

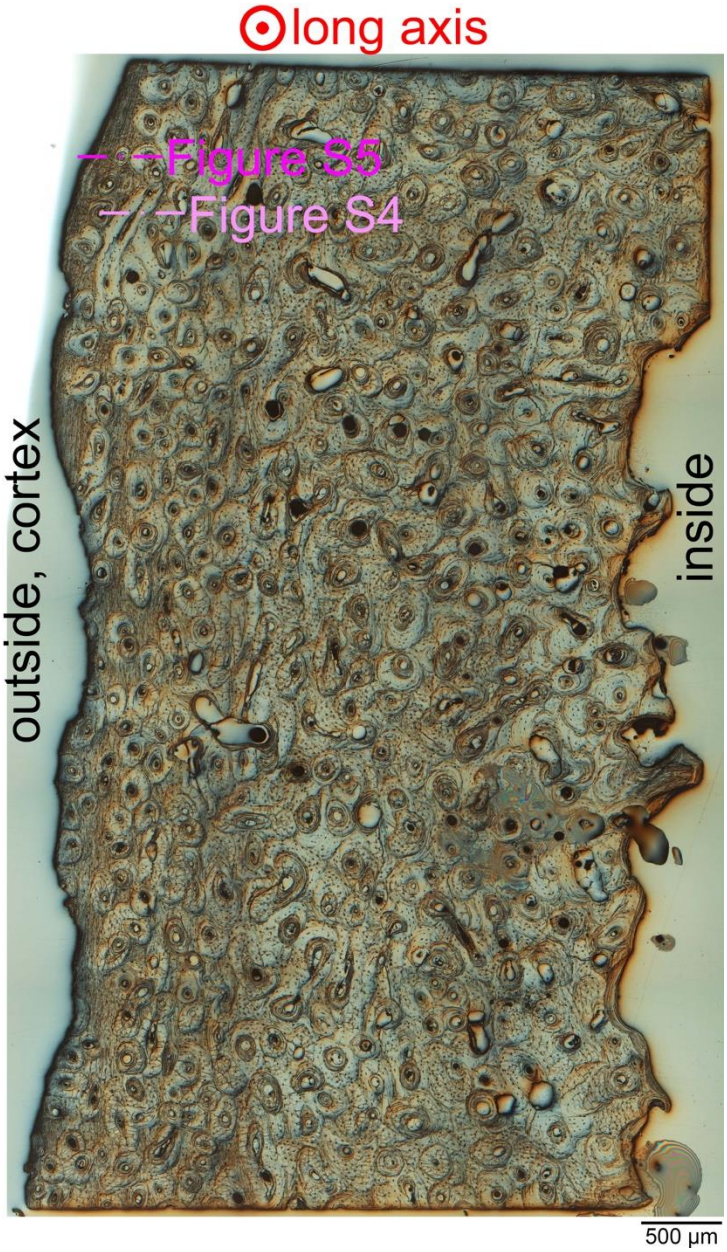

Figure S6. Human bone cut perpendicular to the bone long axis.
Pink and magenta squares to the left of the pink and magenta text, bracketed by horizontal lines, indicate the precise position and size of the areas magnified and analyzed in Figures S4 and S5.

DETAILED METHODS

All L-edge data and images presented here were acquired on beamline 11.0.1.1 PEEM-3 at the ALS, the K-edge data on beamline 10.3.2 also at the ALS.

The various methods used were described throughout the text, with a few exceptions: sample preparation, overabsorption in K-edge spectra, SEM analysis, the alignment of PEEM image stacks, and masking of bone PIC maps. These are described below.

SAMPLE PREPARATION

Two bone samples were prepared from the same 73-year old male human femur. Both were cortical bone, extracted from the femoral mid-diaphysis, one cut longitudinally (Figure S3) and one transversally (Figure S6). The two samples were first embedded in EpoFix (EMS, Hatfield, PA), polished, then re-embedded to fill surface holes by adding a drop of epoxy on the polished surface, and then re-polished to approximately the previous surface, using 300 nm and then 50 nm alumina suspensions (Buehler, Lake Bluff, IL), saturated with phosphate to prevent apatite nanocrystal dissolution.

The mouse incisor from wild type *Mus musculus*, was cut along the midsagittal plane, embedded, and polished as above.

After polishing, All 3 bone and mouse tooth samples were coated with 40 nm around it, and 1 nm Pt within the area of interest, as described previously [2].

The geologic FAP (Yates Mine, Otter Lake, Quebec, Canada) sample was cut with a diamond saw and embedded with the crystallographic *c*-axis in plane in a known orientation. It was then polished as above, but not coated as only X-ray fluorescence experiments were done with it.

OVERABSORPTION IN K-EDGE SPECTRA

Fluorescence-mode XANES spectra on concentrated materials are frequently affected by the phenomenon known as "self-absorption" (a common misnomer) or "overabsorption" [3]. In order to deal with this effect, we mounted the crystal so that the X-ray beam was normally-incident on the sample and fluorescence photons were collected at grazing exit [4] using a relatively small detector (5-mm-diameter Si drift diode). Since the X-ray polarization was horizontal on the 10.3.2 beanding-magnet beamline, mounting the crystal with the *c*-axis horizontal or vertical yielded data for parallel or perpendicular polarization, respectively. These are shown as black and red, respectively, in Figure 2B.

SEM ANALYSIS

SEM images of the bone sample cut along the bone long axis were acquired in backscattered mode with a Versa 3D Dual Beam microscope (FEI, Eindhoven, the Netherlands) equipped with a Concentric Backscattered detector (DBS). The microscope was operated in analytical mode at an accelerating voltage of 20 kV. The sample was coated with a thin layer of C before SEM analysis to avoid charging effects.

Ca SPECTROSCOPY

For Ca movies, that is, stacks of 121 PEEM images were acquired across the Ca L-edge, between 340 eV and 360 eV, with 0.1 eV steps in the central 10 eV and 0.5 eV steps in the featureless pre- and post-edge energy regions. All images were aligned in space using the alignment tool in PeemVision [5]. Spectra were then extracted from single pixels, aligned in energy, and averaged using the GG-Macros [6].

POLARIZATION-DEPENDENT IMAGING CONTRAST (PIC) MAPPING

For PIC maps 38 images were acquired at 19 linear polarization angles, between 0° and 90° with 5° steps, and two anti-correlated energies for each polarization angle. For the bone samples the anti-correlated energies were +0.2 eV above the peak 1 position and -0.2 eV below it for bone samples (as in Figures 3, S1, S2, S4, S5). For the enameloid samples the anti-correlated peaks were peaks 1 and 2, thus we acquired images at 352.6 eV and 351.6 eV.

In both cases we did a digital ratio of the two images acquired at anti-correlated energies, using PeemVision [5]. This yielded the maximum possible dichroic imaging contrast at each polarization. A stack of 19 such image ratios was then used to produce the PIC maps using the Polarization Macro in the GG Macros [6]. As for Ca movies, for PIC maps all images were aligned in space using the alignment tool in PeemVision [5], then digital ratios calculated, and stacks created.

MASKING OF BONE PIC MAPS

For the areas in areas in Figures 3, S1, and S2, a qualitative calcium concentration map was created by dividing the average of 7 on-peak images acquired around 352.6 eV (peak 1) by the average of 9 images acquired in the pre-edge, around 345 eV.

In Adobe Photoshop® CC 2017, the brightest pixels corresponding to greatest Ca concentration were selected by thresholding the image and masking anything below a certain 8-bit grayscale value in black. The specific level was chosen so

that areas containing mostly noise were not visible. For both areas in Figures 3, S1, and S2, the threshold grayscale level was 190.

In the mask image, pixels brighter than the threshold grayscale level were white. These were selected with the magic wand in Photoshop, and deleted, so high-Ca pixels were transparent. When overlapped and aligned to the PIC map, the mask revealed orientation information corresponding to the brightest pixels only.

FDMNES CALCULATED SPECTRA

The FDMNES code (January 19th, 2018 version) was used to calculate the individual Ca L-edge XANES spectra of the four Ca sites present in fluorapatite (FAP). The Green's formalism approach, within the limit of the muffin-tin approximation, was used. The Fermi energy was determined self-consistently using an aggregate of radii of 7 Å. A cluster of 7 Å radius was also used to perform the final state calculations. The Hedin-Lundquist potentials [7] were used to model the exchange-correlation. Dipoles, core-hole contributions and spin-orbit coupling were taken into account.

We have shown only the L_2 edge (peaks 1 and 2) calculated spectra because, as shown in Figure 1A, the experimental L_3 (peaks 3 and 4) is less sensitive to polarization, and thus exhibits lower dichroism. The spectra for the L_3 edge were calculated but since they provide no additional information compared to L_2, they were not presented.

SUPPORTING REFERENCES

(1) Allen, R.; David, G. *Z Wiss Mikrosk Mikrosk Tech* **1969**, *69*, 193.
(2) De Stasio, G.; Frazer, B. H.; Gilbert, B.; Richter, K. L.; Valley, J. W. *Ultramicroscopy* **2003**, *98*, 57.
(3) Goulon, J.; Goulon-Ginet, C.; Cortes, R.; Dubois, J. *J Physique* **1982**, *43*, 539.
(4) Brewe, D.; Bouldin, C.; Pease, D.; Budnick, J.; Tan, Z. *Rev Sci Instrum* **1992**, *63*, 3298.
(5) PeemVision *http://xraysweb.lbl.gov/peem2/webpage/Tools.shtml* **2018**.
(6) GG–Macros *http://home.physics.wisc.edu/gilbert/software.htm* **2018**.
(7) Hedin, L.; Lundqvist, B. I. *J Phys C: Solid State Phys* **1971**, *4*, 2064.